

Atomistic investigation of irradiation-induced defect dynamics in FeNiCu medium-entropy alloy: effect of local chemical order

Kazi Tawseef Rahman¹, Mustofa Sakif Shahriar¹, Mashaekh Tausif Ehsan¹, Mohammad Nasim Hasan^{1*}

¹Department of Mechanical Engineering, Bangladesh University of Engineering and Technology (BUET), Dhaka-1000, Bangladesh.

*Corresponding author *Email address: nasim@me.buet.ac.bd*

Email: 2000tawseef@gmail.com, sakif11902117@gmail.com, mashaekh.tausif@gmail.com, nasim@me.buet.ac.bd

***Corresponding Author:**

Prof. Mohammad Nasim Hasan

Department of Mechanical Engineering

Bangladesh University of Engineering and Technology (BUET)

Dhaka-1000, Bangladesh

E-mail: nasim@me.buet.ac.bd

Telephone: +8801921506445

Atomistic investigation of irradiation-induced defect dynamics in FeNiCu medium-entropy alloy: effect of local chemical order

Abstract: Medium and high-entropy alloys (M/HEAs) have garnered significant attention as potential nuclear structural materials due to their excellent stability at high temperatures and resistance to radiation. However, the common use of Co in M/HEAs, which exhibits high radioactivity under radiation has prompted the development of Co-free M/HEAs for nuclear applications. In this study, we investigate the irradiation behavior of FeNiCu, a promising Co-free medium-entropy alloy (MEA) with a focus on the effect of local chemical order (LCO) using hybrid-molecular dynamics and Monte Carlo simulations. Considerable LCOs in Cu-Cu and Fe-Ni pairs were observed in the thermodynamically stable ordered system. To conduct a comprehensive comparative study of irradiation-induced defect formation and dynamics, cumulative displacement cascades up to 500 were performed in random and ordered configurations of the MEA as well as in pure Ni for benchmark. Our study revealed LCO configuration as the most radiation resistant structure among the three. Complex potential energy landscape (PEL) in MEAs disrupts dislocation growth resulting in its dispersed distribution. The Cu-rich uniform regions in the ordered system act as defect traps enabling faster diffusion and high defect recombination resulting in formation of the dislocation networks in/near these regions. The lower stair-rod dislocation density in the ordered system revealed its high resistance to irradiation swelling signifying the effect of LCO even more, positioning FeNiCu MEA as a strong candidate for future nuclear application. Additionally, the theoretical insights into defect evolution covering formation and diffusion in both random and ordered structures enhance our understanding of LCO's impact, offering a solid foundation for the future development of radiation-resistant M/HEAs for nuclear applications.

Keywords: Molecular Dynamics, Displacement Cascade, Irradiation-induced defects, Local Chemical Order, Medium and High-Entropy Alloys.

1. Introduction

Nuclear energy is the key to a better future, reducing greenhouse gas emissions and providing a consistent and clean energy supply as the world's energy demand is growing continuously [1]. In future, fourth-generation nuclear reactors will need to work in extremely corrosive environments with significant radiation doses and temperatures [2]. For this, the next generation of nuclear materials must have higher corrosion and wear resistance, dimensional stability under radiation, and improved radiation resistance. One of the most promising alternatives that meet all these criteria is medium-entropy alloys (MEAs, with three alloying elements) or high-entropy alloys (HEAs, commonly containing five or more alloying elements) denoted as M/HEA [3]. M/HEAs have gained massive attention for their exceptional qualities, including high strength [4] and hardness [5], superior thermal properties [6], radiation resistance [7], high tensile ductility [8], excellent corrosion [9] and wear resistance [10]. A recent review highlighted that reduced thermal conductivity, sluggish diffusion, and effect on defect energetics are the most commonly cited reasons for better radiation response in M/HEAs [3]. However, some of these proposed reasons remain subjects of ongoing debate. Reduced thermal conductivity in M/HEAs causes slower energy dissipation, leading to a longer thermal spike, which enables increased defect recombination [11]. That is why M/HEAs for nuclear applications have emerged as a hot topic for researchers in recent years.

When compared to elemental materials like nickel (Ni), M/HEAs exhibit superior radiation resistance. Recently in a molecular dynamics (MD) study, Li et al. simulated the evolution of defects during primary irradiation damage and found that CoCrCuFeNi HEA has better performance at inhibiting defect growth than elemental Ni [12]. Another study by Li et al. on CoNiCrFeMn HEA concluded that in contrast to Ni, CoNiCrFeMn shows fewer defects and dislocation loops due to high defect recombination as a result of having a lower difference in migration energy between interstitial and vacancy [13]. Similar behaviors were observed by Lin et al. with NiCoCrFe HEA [14] and Lang et al. with NiCoFe MEA [15]. In an experimental study by Yaykaşlı et al., a novel HEA composition $\text{Co}_{0.2}\text{Cr}_{0.2}\text{Fe}_{0.2}\text{Ni}_{0.2}\text{Ag}_{0.2}$, fabricated through mechanical milling process, showed thermal stability and excellent radiation shielding properties [16].

While the radiation resistance of M/HEAs has been a major focus of research, their exceptional performance cannot be attributed solely to their random atomic configuration. Originally, M/HEAs

were believed to form random solid solutions (RSSs) with homogeneous atomic distributions. However, recent research has shown that local chemical order (LCO) with heterogeneous mixture is another important feature of M/HEA [17,18]. By adjusting the alloy fabrication processing conditions, LCO can be tunable, which has a substantial impact on the defect energetics and consequent changes in mechanical characteristics [19]. Hence, LCO has recently gained attention as a research area, particularly due to its effect on the mechanical properties of M/HEA [20,21]. For instance, Cantor alloy CoCrFeMnNi, previously considered as a single-phase solid solution has been shown to form a secondary Cr-rich precipitated phase after prolonged annealing at certain temperatures [22,23]. Some studies have also reported LCO in CrCoNi MEA [17,24]. Furthermore, LCO has been found to increase stacking fault energy (SFE) in M/HEAs which has a significant impact on mobility of dislocations and growth of defects [21]. However, measuring LCO and defects, especially analyzing their dynamic behavior, has been proven to be challenging in experimental research. Therefore, numerical simulations have been lately an effective way to study the effect of LCO on the irradiation resistance of M/HEA. Recently two separate MD studies by Liu et al. and Arkoub and Jin on FeNiCr MEA showed considerable LCOs consisting of Cr-Cr and Ni-Fe short-range order (SRO) which had a significant effect on defect and dislocation characteristics [25]. Li et al. showed delayed defect growth in the ordered structure of CoNiCrFeMn HEA and reduced dislocation density, suggesting better radiation resistance [26]. However, a study by Koch et al. using CuNiCoFe MEA revealed almost little to no effect on radiation resistance, raising doubts about the reduced effect of radiation owing to LCO [27]. Thus, further study is needed to fully understand the effects of radiation resistance due to LCO on M/HEAs.

In addition to understanding the role of LCO, there has been a growing interest in Co-free M/HEAs. Co, commonly used in many HEAs, poses challenges in nuclear applications due to its high activation energy under irradiation, which makes it highly radioactive and difficult to handle. This necessitates additional radiation shielding and increases the risk of contamination in the reactor's primary coolant circuit if it leaches into the water [3]. As a result, researchers are focusing on developing Co-free M/HEAs [28,29]. In this context, Cu-containing M/HEAs have emerged as a promising alternative for nuclear applications [30], with FeNiCu MEA being a material of particular interest. The MEA shows similar hardness and even superior tensile strength compared to another Cu-containing MEA CuCrZr, which is being considered as heat sink material for ITER

first wall and divertor [31], making it a potential candidate for nuclear applications. However, further prolonged irradiation damage studies are needed to assess its irradiation resistance, as no such investigations have been conducted to date, to the best of the author’s knowledge.

In this work, we focused on investigating both the random (RSS) and ordered (LCO) structure of FeNiCu as Cu has a tendency to precipitate and form Cu-rich domains in alloys [32]. We employed a hybrid MD and Monte Carlo (MC) simulation to explore the effects of LCO on defect dynamics and energetics. MC simulations were applied to achieve an LCO containing configuration of FeNiCu MEA. To investigate the prolonged irradiation damage and defect dynamics, large-scale MD simulations with up to 500 successive displacement cascades were carried out in both RSS and LCO configurations. For comparison, elemental Ni was also simulated. We analyzed and compared defect and dislocation evolution across RSS, LCO, and Ni systems as the irradiation cascade progressed. Our findings provide insights that can aid in the development of future structural materials for nuclear applications and offer a fresh perspective on the impact of LCO on radiation damage behavior.

2. Methodology

2.1 Simulation Cell and Interatomic Potential

All the simulations in our current work were carried out using MD software LAMMPS, which is a widely recognized open-source MD simulator [33]. The simulation cell size was set to $30a_o \times 30a_o \times 30a_o$, where a_o is the face-centered cubic (FCC) lattice constant, resulting in a system containing 108,000 atoms. The lattice constants for Ni and FeNiCu were 0.352 nm and 0.355 nm, respectively. Calculation details of equilibrium lattice constant for FeNiCu MEA can be found in **Supplementary Note 1**. The pure Ni and random configuration of FeNiCu were prepared using AtomsK software [34]. Equiatomic Fe, Ni, and Cu atoms were randomly placed on the FCC lattice sites in the RSS configuration. The LCO configuration of FeNiCu was created using hybrid MC/MD simulation to achieve an energy-minimized ordered system. The specific procedure for this is detailed in **section 2.2**. To describe the force field of the simulation system, we employed the embedded-atom method (EAM) potential developed by Tramontina et al. [35]. This potential is a modified version of Bonny et al. [36] which comes with Ziegler–Biersack–Littmark (ZBL) [37] modification for short-range interactions, making it suitable for radiation cascade studies. The mathematical model for EAM potential is as follows:

$$E_i = \sum_{j \neq i} F_\beta \rho_\gamma(r_{ij}) + \frac{1}{2} \sum_{j \neq i} \varphi_{\beta\gamma}(r_{ij}) \quad (1)$$

Here E_i is the potential energy of atom i , r_{ij} is the distance between atoms i and j , $\varphi_{\beta\gamma}$ is a pair-wise potential function, ρ_γ is the contribution to the electron charge density from atom j of type γ at the location of atom i , and F is an embedding function that represents the energy required to place atom i of type β into the electron cloud. To quantify the local chemical ordering, we used the Warren–Cowley parameter [38], which is formulated as follows:

$$\alpha_{ij}^m = 1 - \frac{p_{ij}}{c_j} \quad (2)$$

Here α_{ij}^m is the Warren–Cowley parameter for the m -th nearest neighbors' shell and p_{ij} is the average probability of finding a j -type atom in the system. A negative α_{ij}^m suggests the tendency of j -type clustering in the m -th nearest neighbors' shell of an i -type atom, while a positive value means repulsion. In our work, we have only calculated α_{ij}^1 , which is the Warren Cowley parameter for the first nearest neighbors (1NNs) shell. From now on, we will denote α_{ij}^1 as α_{ij} for simplicity. The code written by Sheriff et al. [39] was used in our study to calculate α_{ij} .

2.2 Hybrid MC/MD Simulation

The energy-minimized LCO configuration is obtained by annealing the RSS system using hybrid MC/MD simulation. On each MC step, the two different types of atoms are swapped places to slowly minimize the total potential energy of the system. The acceptance to each MC swap confirms to Metropolis criterion [40]. If the system energy, E_{i+1} following the $i+1$ -th swap attempt is lower than the system energy, E_i from the previously accepted swap. Otherwise, it is accepted with a probability:

$$P = \exp\left(\frac{E(i+1) - E(i)}{k_B T}\right) \quad (3)$$

Here T is the chosen temperature of the system and k_B is the Boltzmann constant. The MC swap is allowed if a uniformly generated random number R in the interval $(0,1)$ is less than or equal to P . Our RSS system was annealed at 300 K temperature by performing one MC step followed by one MD step of isothermal-isobaric ensemble (NPT) with a timestep of 1 fs. This process was continued for 430 ps resulting in 215,000 MC steps and 63389 accepted swaps. On each MC step,

10 trial attempts were made and periodic boundary conditions were applied in all three dimensions of the simulation cell. **Fig. 1(a)** shows how, the system's potential energy is decreased as the annealing process proceeds. After 430 ps, we get our thermodynamically stable LCO configuration. During the process, the Cu atoms slowly segregate which is also seen in other literature [32]. Cu-rich domains are clearly seen in **Fig. 1(c)** in the LCO system. To quantify the ordering, we calculated α_{ij} of all the pairs and the results coincide with **Fig. 1(b)**, indicating significant LCO in the Fe-Ni and Cu-Cu pairs. Whereas α_{ij} for RSS are all nearly zero, meaning a random mixture with no ordering. We also performed hybrid MC/MD simulations at different annealing temperatures and found that dominant chemical orderings (Fe-Ni and Cu-Cu atomic pairs) have no significant change with temperatures (see **Supplementary Note 2**).

2.3 MD Displacement Cascade Simulation

To study the prolonged irradiation damage in the Ni, RSS, and LCO systems, we performed 500 consecutive displacement cascades which corresponds to a radiation dose of ~ 0.23 dpa (calculated based on the NRT model with a threshold displacement energy 40 eV [41]). The short simulation time between collision cascades, which is a restriction of MD, results in a dosage that is far larger than experimental settings. Before the displacement cascades were performed, each system was relaxed for 100 ps under isothermal-isobaric ensemble (NPT) at 300 K and zero pressure conditions. An atom is randomly chosen as the primary knock-on atom (PKA) and the entire cell was shifted under periodic conditions to move the PKA at the center. This was done to ensure that the PKA doesn't reach the cell boundaries. Then the PKA was given a velocity equivalent to 5 keV of kinetic energy in a random direction. Adaptive timestep was adopted during the entire cascade process. The Nose-Hoover temperature-rescaling thermostat [42,43] was applied on the boundaries (thickness of 3.6 \AA) to act as a heat sink and cool down the system to 300 K with a damping parameter 100 times the adaptive timestep. The interior of the simulation system was under microcanonical ensemble (NVE). Each cascade was run for 23,000 adaptive timesteps (around 44 ps) which was enough to cool down the entire system to 300 K. To eliminate any drifting of the system during cascade simulation, the center of mass of the entire system was constrained to its initial position. After each cascade, the simulation cell was shifted back to its original position under periodic conditions in order to allow analysis, which uses the original location of the simulation cell as reference. This process is repeated 500 times to achieve the

prolonged irradiation damage. The adaptive timestep was changed between 0.0001 to 2 fs such that atomic movement was limited to 0.1 Å and atomic energy change was limited to 2.5% of PKA energy. The electron stopping effect was taken into account for the atoms with kinetic energies more than 10 eV. The electron stopping powers were calculated using the SRIM software package [44]. Other details of the simulation procedures can be found elsewhere [17,45]. To get more statistically reliable findings, three independent simulations were run for each system using different seed values for prolonged displacement cascades. Meanwhile, to study the defect evolution with time in a single cascade event, 30 independent simulations were run for each system.

2.4 Defects Analysis and Visualization

To analyze the damage at the end of each cascade, the irradiated system is compared with the initial relaxed structure. All the visualization and analyses were done using the OVITO software package [46]. Wigner-Seitz cell method with Voronoi polyhedral was used to detect the point defects in the system. Polyhedra with more than one atom were identified as interstitials, and no atoms as vacancies. Defect clusters were analyzed with Cluster Analysis method with a cut-off radius equal to the second nearest neighbor distance. The dislocations were identified and analyzed with Dislocation Analysis (DXA) method.

2.5 Chemical Potential Calculation

To calculate vacancy and interstitial formation energy, chemical potentials of the elements in the system are required. In our work, chemical potentials were calculated using Widom-type substitution techniques [47]. We calculated the different chemical potentials of elements present in a system by randomly substituting one type of atom with another type:

$$\mu_A - \mu_B = \frac{1}{2}(E^{A \rightarrow B} - E^{B \rightarrow A}) \quad (4)$$

$$\mu_B - \mu_C = \frac{1}{2}(E^{B \rightarrow C} - E^{C \rightarrow B}) \quad (5)$$

$$\mu_C - \mu_A = \frac{1}{2}(E^{C \rightarrow A} - E^{A \rightarrow C}) \quad (6)$$

Here μ_A , μ_B , and μ_C are the chemical potentials of the atom types A, B, and C respectively. $E^{A \rightarrow B}$ is the energy of the system after a B-type atom is substituted with an A-type atom (similar expressions apply for the other cases). For calculation, we need another equation, which is:

$$E_o = N_A \mu_A + N_B \mu_B + N_C \mu_C \quad (7)$$

Where, E_o is the initial system potential energy without any substitution and N_A , N_B , and N_C are the number of atoms of type A, B, and C respectively. With these equations, we have calculated the values of μ_{Fe} , μ_{Ni} , and μ_{Cu} for Ni, RSS, and LCO. We used a FeNiCu system containing 864 atoms with equiatomic composition and performed 288 substitutions of each type for all the alloys, which covers the substitution of all atoms of a certain type in the system. Further details can be found elsewhere [48,49]. To generate an equivalent LCO structure in the 864-atom system, the same number of accepted Monte Carlo swaps per atom (~ 0.59) was performed as in the original 108,000-atom LCO structure, using MC/MD simulation.

2.6 Vacancy and [100] Interstitial Dumbbell Formation Energy Calculation

Vacancies are created by randomly removing one atom from the system and [100] Interstitial dumbbells are created by randomly replacing one atom with a pair of atoms equidistant from the lattice site in [100] direction. The formation energies are calculated by subtracting the potential energy of the perfect system from the potential energy of the defected system. The imbalance of the total atoms in the initial and final systems is compensated using the chemical potential:

$$E_f = E_d - E_o \pm \mu \quad (8)$$

Here E_f is the corresponding formation energy of the defect, E_o is the energy of the perfect system, E_d is the energy of the defected system and μ is the chemical potential of the extra atom added or deleted. For vacancy, the chemical potential is added and for dumbbell, it is subtracted. 1000 calculations were performed for each type of point defects. Conjugate Gradient energy minimization method was used while calculating the energies.

2.7 Defect Migration Energy Barrier Calculations

Migration energy barriers were determined using the Climbing Image Nudged Elastic Band (CI-NEB) method [50]. Point defects were created using the method described in the previous section. The vacancies were exchanged with all the 12 1NNs, thus all the possible 12 pathways were

considered for each vacancy during the vacancy migration energy calculation. A total of 10368 calculations were performed to get statistically accurate results. For interstitials, we rotated [100] dumbbells to [010] dumbbells on the {001} plane using the shift and rotate mechanism [51]. As rotating interstitial dumbbells doesn't always result in intended rotation in alloys because of high lattice distortion, the dumbbell migration energies were calculated using migration energies of pure structures and dumbbell formation energies [48]:

$$E_m^{A-B-C} = E_m^B - E_f^{A-B} + E_f^{B-C} \quad (9)$$

Here E_m^{A-B-C} is energy barrier of rotating a [100] A-B dumbbell to [010] B-C dumbbell (B is the extra added interstitial atom). E_m^B is the dumbbell migration energy of pure B, E_f^{A-B} and E_f^{B-C} are the formation energies of dumbbells A-B and B-C respectively. If the dumbbell type remains unchanged after rotation, the migration energy is simply taken as the migration energy of the pure system of the interstitial atom:

$$E_m^{A-B-A} = E_m^B \quad (10)$$

If the migration energy was negative, it was replaced by a small value (0.001 eV). Migration energies of all the 27 types of dumbbells (9 different combinations for each of the 3 types of interstitial atoms) that can be found in FeNiCu alloys, were calculated. To get converged CI-NEB results, EAM potential by Deluigi et al. [52] was used to calculate the dumbbell migration energies of pure systems. All the pure systems were considered FCC structures. For vacancy migration calculations, the small RSS and LCO structures mentioned in **section 2.5** were used. As for dumbbell migration calculations in pure systems, corresponding energy-minimized pure systems consisting of 2049 atoms were used. All the CI-NEB calculations were performed with 12 system replicas, including the initial and final states. The force tolerance convergence criterion and the spring constant were set to 0.005 eV/Å and 1 eV/Å respectively [25]. Examples of CI-NEB computed point defect migration minimum energy pathways (MEPs) can be found in **Supplementary Note 3**.

3. Results and Discussion:

In this study, the effects of LCO on irradiation-induced defect evolution in FeNiCu MEA were investigated using hybrid MC/MD simulations. We analyzed defect formation, dislocation

dynamics, and atomic diffusion in both random and ordered configurations, with pure Ni as a reference. Key metrics such as number of Frenkel pairs, formation energy, migration energy, and dislocation density were used to assess radiation resistance across multiple displacement cascades.

3.1 Initiation and Development of Point Defects

Point defects like interstitials and vacancies start to develop as the PKA collides with other atoms. The evolution of point defects in a single displacement cascade for pure Ni and M/HEA can be described in four stages. The first phase is known as the ballistic phase where the number of Frenkel Pairs (N_{FP}) increases at a sharp rate. **Fig. 02(a)** shows that this phase lasts for ~ 0.12 ps. During this period, little to no difference among Ni, RSS, and LCO is observed. Then starts the PKA energy depletion phase and lasts till 1 ps. During this phase, defect peak is observed. It is seen that for Ni the peak occurs earlier than the MEAs due to the fact that H/MEAs generally have lower thermal conductivity than pure Ni. Higher thermal conductivity in Ni enables quick transfer of energy throughout the lattice sites which leads to rapid energy dissipation resulting in a shorter energy depletion phase. Meanwhile, the more complex atomic environment in MEAs scatters the phonon more efficiently resulting in lower thermal conductivity which hinders the energy dissipation leading to a longer localized thermal energy peak. Therefore, a prolonged energy depletion phase is obtained. Furthermore, it is also observed that Ni has a lower defect peak than MEAs. The third stage, known as the recombination phase, is when the N_{FP} starts to rapidly drop. In the third phase, fast atom mixing is made possible by the formation of a localized molten zone at the structure's core following the defect peak. This atomic mixing rate physically correlates with the atomic diffusivity and cohesive energy in the molten phase of the structure [53]. We have examined this atomic mixing for the three cases in **Fig. 10(a)**. The mixing is quantified by mean squared displacements (MSD) of all atoms in the system with the initial relaxed system as reference:

$$MSD(t) = \frac{1}{N} \sum_{i=1}^N \langle |r_i(t) - r_i(0)|^2 \rangle \quad (11)$$

Here $r_i(0)$ and $r_i(t)$ are the coordinates of i -th atom at the initial and current time respectively. In **Fig. 10(a)**, it is clear that in all cases, the atomic mixing is strongly linear as a function of cumulative displacement cascade number. Pure Ni shows a lower mixing rate compared to MEAs. This is because pure Ni is a highly ordered, crystalline structure, leading to quick return of atoms to their equilibrium positions after displacement resulting in lower MSD. Also, the higher thermal

conductivity of Ni plays a significant role here as it enables quicker heat dissipation resulting in faster solidification of the localized molten phase. So, atoms get a shorter period to diffuse. Whereas the complex atomic environment in MEA with lower thermal conductivity enables longer solidification time resulting in higher atomic diffusion. Additionally, the mixing rate of LCO is seen as lower than the RSS configuration. This indicates that the effect of LCO is significant in atomic mixing because the strong and uniform Cu-Cu bonds in Cu-rich domains supposedly decrease the overall diffusion of atoms resulting in lower atomic diffusivity in the molten phase. With time, N_{FP} decreases as interstitial and vacancy defects recombine. This recombination phase lasts till ~ 1.6 ps. After this, a plateau stage is reached where only the surviving Frenkel Pairs remain. It is seen that pure Ni has more surviving defects than RSS and LCO, yet both have comparable amounts of residual defects. The recombination rates of the three structures are shown in **Table 1** which can be evaluated as:

$$\% \text{ Recombination} = \frac{N_{peak} - N_{end}}{N_{peak}} \times 100\% \quad (12)$$

Here N_{peak} is the peak N_{FP} and N_{end} is the surviving N_{FP} at the end of the first cascade event. We see that Ni has the lowest defect recombination rate whereas LCO and RSS have similar recombination rates.

Even though we see little to no difference between the RSS and LCO configurations in the first cascade event, the effect of LCO is prominent in prolonged displacement cascades. In **Fig. 2(b)**, it can be seen that the N_{FP} linearly increases as the number of cascades (N_C) increases till ~ 35 cascades. After that, we see a non-linear behavior in defect progression. The non-linearity is caused by overlapping displacement cascades where the debris of a cascade affects the next cascade [54]. The growth of defects in the alloy slows down after linear region, but it still grows at a significant rate in Ni making MEA more irradiation resistant. We see significantly less defect growth in the LCO than in RSS after ~ 110 cascades. So, it is clear that LCO has a significant impact on defect production in FeNiCu MEA. Detailed analysis to understand the better irradiation performance in MEA, especially in the ordered configuration, is conducted in the following sections.

3.2 Defect Energetics

To understand the defect characteristics and effect of LCO in FeNiCu MEA, point defect formation and migration energies are calculated. Formation energies indicate the point defect's formation

difficulty. A higher formation energy indicates a higher formation difficulty and vice-versa. In pure Ni, vacancy formation energy (E_f^v) is constant at 1.56 eV. However, **Fig. 3(a-f)** illustrates a distribution of E_f^v in RSS and LCO as a result of the structures' diverse local compositions. Compared to RSS, LCO exhibits greater E_f^v for all types of vacancies, though these values remain lower than that of pure Ni. This increase in E_f^v values due to ordering in LCO explains the lower N_{peak} compared to RSS observed in **Fig. 2(a)** as fewer vacancies form in more thermodynamically stable structures. When comes to interstitial defects, it is seen that [100] dumbbell is the most energetically favorable interstitial defect in pure Ni compared to octahedral, tetrahedral, and crowdion interstitials [51]. So, we only calculated the energetics of [100] dumbbells in our present work for consistency. Compared to Ni, which has a constant interstitial dumbbell formation energy (E_f^i) of 4.63 eV, RSS and LCO have lower values for different types of dumbbells as seen in **Fig. 4(a)**. This variation of formation energies provides insight into the trends observed in the previous section. Since Ni has higher defect formation energies (for both vacancies and interstitials) than RSS and LCO, the N_{peak} is lower in Ni compared to RSS and LCO alloys. In particular, LCO exhibits lower interstitial formation energies and higher vacancy formation energies compared to RSS. These results align with the findings of Arkoub and Jin [53] in FeNiCr MEA. Moreover, a significant difference is noticed between E_f^v and E_f^i where E_f^v being considerably lower than E_f^i , indicating that interstitials are harder to form than vacancies. Furthermore, it is evident from the figures that in LCO, Cu-containing point defects are easier to form as both the vacancy and interstitial formation energies are lower compared to others. The average E_f^i of Cu-X dumbbells (where X = Cu/Fe/Ni) is 3.22 eV being substantially lower than other dumbbell pairs. This is a result of the comparatively uniform potential energy landscape (PEL) provided by the Cu-rich regions in the LCO structure, where the local lattice distortion is lower than in other areas. This promotes the easier formation of defects in these domains.

Meanwhile, formation energies explain the N_{peak} , they don't explain the recombination of Frenkel pairs. Therefore, migration energies are calculated. Migration energies are an indicator of point defects' diffusivity. Lower migration energy means higher diffusivity and vice-versa. Pure Ni has a constant vacancy migration energy (E_m^v) of 0.98 eV and a constant dumbbell migration energy (E_m^i) of 0.178 eV which agrees well with the values found in other computational and experimental studies [49,55,56]. Meanwhile, **Fig. 3(g-h)** and **Fig. 4(b)** show migration energy distributions of

point defects in RSS and LCO. Again, the wide energy distribution was obtained because of the diverse localized composition in MEAs. E_m^v of Fe, Ni, and Cu are 0.99 ± 0.18 eV, 1.07 ± 0.18 eV, and 0.77 ± 0.13 eV respectively in RSS and 1.09 ± 0.23 eV, 1.19 ± 0.29 eV and 0.73 ± 0.15 eV in LCO. While the migration barrier increases for Fe and Ni vacancies in LCO compared to RSS, Cu shows the opposite trend. This is because of the uniform Cu-rich regions in LCO where the migration barrier gets close to that of pure Cu which is a constant 0.70 eV. Moreover, average E_m^i of interstitial atoms Fe, Ni, and Cu are found to be 0.154 eV, 0.180 eV, and 0.106 eV respectively in RSS and 0.172 eV, 0.246 eV, and 0.150 eV in LCO. The overall increase in both vacancy and interstitial migration energies can be explained by the roughened PEL because of the developed ordering in the LCO system [57]. Higher diffusivity of Cu in alloys indicated by lower vacancy and interstitial migration energies is also observed in other studies [58,59] which aligns with our findings. Individual calculated migration barrier values for all 27 types of dumbbell rotations can be found in **Supplementary Note 4**. Overall, the interstitial migration energies are found to be substantially less than that of vacancies suggesting higher diffusivity of interstitials compared to vacancies. Therefore, interstitial defects will have a higher tendency to form clusters than vacancies which will be discussed in detail in **section 3.3**.

3.3 Transition of Point Defects to Defect Clusters

With the cut-off radius being set as second neighbor distance, every point defect within the range was considered to be a member of the same defect cluster. The term cluster size is used to indicate the number of defects within a cluster. Clusters containing 2-30, 31-100, and 100+ point defects were defined as small, medium, and large clusters respectively for interstitial clusters. Whereas clusters containing 2-10, 11-30, and 30+ point defects were defined as small, medium, and large clusters respectively for vacancy clusters. In **Fig. 5**, the number of defects involved in a cluster are simply calculated by multiplying cluster number with cluster size. So, increase or decrease in number of defects in a cluster implies corresponding change in cluster numbers. From **Fig. 5**, it is evident that vacancy cluster growth is much more difficult than that of interstitial because of the significant difference in migration energy as discussed in the previous section. Lower migration energies of interstitials allow easier diffusion in the system and accumulate with other interstitials. Whereas the vacancies are more dispersed in the system as seen in **Fig. 7**. In **Fig. 5**, both interstitial and vacancy single clusters shows an approximate increasing trend with increasing number of

cumulative cascades in all the systems where Ni shows the lowest numbers for interstitials and the opposite for vacancies. Small and medium interstitial clusters are significantly low for Ni compared to the MEAs. As for alloys, medium interstitial clusters grow steadily at first before showing a sharp decline. Large interstitial clusters are significantly high in Ni compared to alloys, which explains the significantly low numbers of small and medium clusters, as they likely accumulate together and form large clusters. Meanwhile, the large clusters in alloy systems grow at a much lower rate. The rapid fall of medium interstitial clusters in alloy systems explains the delayed growth of large clusters as higher cascade number promotes the growth of large interstitial clusters. The medium clusters combine with each other and forms the large interstitial clusters. Moreover, the number of interstitials in interstitial clusters in LCO is less than RSS in most cases of cluster size, which suggests local ordering inhibits interstitial cluster formation and growth.

As for vacancy clusters, both small and medium-sized clusters grow gradually with the increasing number of cascades in the Ni system. For alloys, small vacancy clusters also gradually increase but medium clusters show a gradual decrease in number after 300 cascades. Large vacancy clusters also grow rapidly in Ni just like interstitial clusters from the very beginning but in a significantly lower number. In contrast, the alloy systems show a much-delayed growth especially the LCO configuration where no large clusters can be seen within 400 cumulative cascades. This strongly suggests higher irradiation resistance in LCO thanks to its roughened PEL and higher migration energies. Lower large vacancy clusters in the alloy systems are a direct indicator of higher resistance to irradiation swelling which is discussed in more detail in **section 3.4**. **Fig. 6** shows the growth of the largest cluster size with increasing displacement cascades. Ni shows around twice the number of interstitial defects and around twice the number of vacancy defects in the largest cluster compared to the alloys. This demonstrates the superiority of MEAs over pure Ni in terms of irradiation resistance. While both RSS and LCO show similar growth, LCO still suppresses the aggregation of interstitial and vacancy point defects a little more than the RSS configuration. The clear details of defect growth and interaction can be seen in the **Supplementary Videos**.

To investigate the number of different constituents in the defect clusters, the percent constituents in interstitial clusters excluding single clusters as a function of cumulative displacement cascade number are plotted in **Fig. 10(c-d)** for RSS and LCO systems. In RSS, the Cu percentage doesn't change much and fluctuates around 0.28%. Whereas a gradual decrease in Ni percentage and a gradual increase in Fe percentage are seen as the irradiation dose increases. This indicates Ni

interstitials are being replaced by Fe interstitials with increasing irradiation dose. This can be explained by the lower interstitial migration energies of Fe interstitials than Ni interstitials seen in **Fig. 4(b)**. Meanwhile, in LCO, the Cu percentage is significantly higher at the beginning than its overall 0.33% composition ratio in the system. This suggests that interstitial defect clusters prefer to locate in Cu-rich domains (more on this in **section 3.4**). But it rapidly decreases as more and more cascade events occur. This indicates the destruction of Cu-rich domains with increased radiation dose. As the Cu percentage decreases in the interstitial clusters, they get replaced with Ni and Fe interstitials which explains the increasing trend of Ni and Fe in **Fig. 10(d)** as the cumulative cascade number increases. Moreover, it seems that the percent constituent in LCO configuration proceeds to reach a common stable value with increasing cumulative cascades.

3.4 Dislocation Characteristics

Dislocation loops are formed due to the aggregating nature of point defects. When the point defects form clusters, dislocation loops start to develop around them. The evolution of dislocations can be characterized in three stages. First is nucleation then growth and lastly forming dislocation networks [25]. In our work, the dislocation loops are identified and analyzed using DXA method. The dislocation distribution in Ni, RSS, and LCO can be seen in **Fig. 7** after 100, 300, and 500 cumulative displacement cascades. From the snapshots of the systems, it is evident that dislocation forms around point defect clusters. Especially the Shockley and Frank dislocations are generally formed around interstitial clusters, while the Stair-Rod dislocations are generally formed around vacancy clusters. It can be seen that, as the number of cascades increases the dislocations also increase. For $N_c = 100$, the Shockley dislocations in RSS and LCO are very dispersed forming small-sized chained loops. While in Ni, a large-sized Shockley dislocation chain is seen. This trend is consistent in $N_c = 300$ and 500 too. This indicates growth of dislocations in MEA is hindered by complex PEL and local chemical compositions and concluding the superiority of MEA over pure structures. Additionally, the snapshots for $N_c = 500$ suggest the growth of Shockley dislocations is even harder in LCO configuration as the dislocations are more dispersed while RSS forms a comparatively large Shockley dislocation chain. This suggests chemical ordering in MEA has a significant impact on dislocation evolution. The dislocation loops grow by absorbing small-sized dislocations (small defect clusters getting aggregated to larger clusters) which agrees with our findings in the previous section. Moreover, it is evident that Shockley dislocation loops form complex chains which agree with other MD studies [12,60]. Meanwhile, Shockley and Frank

dislocations grow very large with consecutive cascades, the Stair-Rod dislocations don't grow that much in comparison. This is because, as mentioned earlier, Star-Rod dislocations are formed by vacancy clusters and vacancy clusters have a lower tendency of aggregation. These findings perfectly align with our results in cluster analysis.

To investigate the evolution of dislocations in greater detail, total dislocation density (ρ_{total}) and Stair-Rod dislocation density (ρ_{sr}) are plotted as a function of cumulative cascade number in **Fig. 8**. In **Fig. 8(a)**, little to no difference is observed in total dislocation density up to 35 cascades among all the systems. If we revisit **Fig. 2(b)**, no difference was also found among the system in the mentioned cascade range because of non-overlapping cascades. It suggests that similar behavior in dislocation density is also related to non-overlapping cascades. After 35 cascades, Ni shows a decrease in dislocation density growth while the previous growth is still consistent in RSS and LCO. This steep growth of dislocation density in RSS and LCO lasts till 100 cumulative cascades where no significant difference is observed between RSS and LCO in terms of dislocation growth behavior. The delayed growth in dislocation density in LCO becomes prominent after 200 cumulative cascades. After 150 cumulative cascades, the growth rate of dislocation density in MEAs becomes minimal, with LCO in particular showing fluctuations around a stable value. In contrast, Ni continues to exhibit a consistent increase in dislocation density until the end. This suggests that over time, pure Ni will develop higher dislocation densities compared to MEAs, aligning with the superior irradiation resistance of MEAs.

A major concern in materials for nuclear applications is irradiation-induced swelling [61]. This swelling is the voids in structures introduced by heavy radiation which is formed by the accumulation of vacancies. The voids are indicated by stacking fault tetrahedral (SFT) which is essentially the ratio of Stair-Rod dislocation segments to six and is an important parameter to assess the irradiation performance of materials [60]. So, to investigate the irradiation-induced swelling, Stair-Rod dislocation density (ρ_{sr}) is shown in **Fig. 8(b)**. Immediately it is evident that the number of SFT in pure Ni is significantly (around three times) higher than MEAs. Which suggests poor irradiation performance of pure Ni structures. Additionally, lower ρ_{sr} is seen in the case of LCO compared to RSS in higher cumulative cascades. This indicates the stacking fault energy (SFE) in ordered structures is higher which agrees with the literature [62,63]. Overall, it can safely be concluded that LCO shows better irradiation performance in terms of dislocation growth.

Moreover, the existence of LCO is supposed to cause high lattice distortion around the ordered regions resulting in significant shear strain. This high shear strain behaves as a catalyst to form dislocation loops leading the ordered regions to act as dislocation nucleation sites [63]. In our case, the prominent ordered regions are the Cu-rich domains. This suggests that dislocations are likely to form in these regions. To investigate this, we have shown the snapshots of RSS and LCO systems at different radiation doses including dislocation lines in **Fig. 9**. It is clearly seen that in LCO configuration, most of the dislocations are formed inside or near the Cu-rich domains. In contrast, no preference is seen for the dislocation formation in RSS configuration. This means in LCO, defects prefer to accumulate in/near Cu-rich domains. This is because these localized uniform regions facilitate the diffusion of defects, thereby acting as effective defect traps. Because outside these regions the PEL is rough thus making it energetically unfavorable for the defects to leave these regions. This trapping effect enables high defect recombination in these regions. Additionally, from the snapshots, a clear destruction of Cu-rich domains is seen as the radiation dose increases. We have quantified the level of Cu ordering using the Warren Cowley parameter for the Cu-Cu bond (α_{Cu-Cu}). **Fig. 10(b)** vividly illustrates that α_{Cu-Cu} in LCO is significantly negative which means a strong Cu-Cu clustering resulting in Cu-rich domains. But as the cumulative cascade increases α_{Cu-Cu} value increases at a decreasing rate. This clearly indicates a decrease in Cu-Cu clustering i.e., destruction of Cu-rich domains due to ballistic collisions and thermal spike atomic mixing. This is why the Cu percentage in the LCO structure decreases as a function of cumulative cascade as seen in **Fig. 10(d)**. Meanwhile in RSS, α_{Cu-Cu} very slowly decreases with cumulative cascade. This suggests ordering is developing at a very low rate in the random structure with increasing radiation dose. This phenomenon is observed in other studies too [64]. Moreover, the degree of order seems to reach an asymptotic/steady state value. This state may be achieved if the simulation is run for beyond 500 cascades. This behavior has also been reported in FeCr alloy under heavy irradiation [65].

4. Conclusion

This study investigates the significant impact of LCO on the irradiation characteristics of FeNiCu MEA compared to RSS and pure Ni using hybrid MC/MD simulations. The ordered LCO configuration demonstrated more radiation resistance as it showed higher degree of defect recombination and reduced defect clustering relative to pure Ni and RSS. The complex atomic environment and diverse local composition in MEA led to uneven PEL resulting distributed defect

energetics. The complex PEL disrupted the dislocation growth in MEA thereby leading to a more dispersed distribution of dislocation networks. In particular, the ordered configuration showed a more dispersed distribution than the random configuration because to the chemical ordering of the system, which roughened the PEL and increased its complexity. Furthermore, the ordered structure demonstrated the lowest Stair-Rod dislocation density, indicating enhanced resistance to irradiation-induced swelling. The Cu-rich regions in the ordered structure acted as effective defect traps which facilitated enhanced defect diffusion and improved recombination. Moreover, the high shear strain around the Cu-rich regions made them act as effective dislocation nucleation sites causing dislocation networks to preferentially form in or near these regions. These findings provide deeper insights into how atomic distribution interacts with radiation damage in M/HEAs. This offers a theoretical framework for designing enhanced radiation resistant materials which is essential for challenging nuclear environments. Future research on Co-free M/HEAs may benefit from the tunability of LCO, which offers promising paths for composition and processing optimization.

Acknowledgement

The authors gratefully acknowledge the high-performance computing facilities provided by the Institute of Information and Communication Technology (IICT) during this study. Additionally, the authors extend sincere thanks to Mahmudul Islam, Doctoral Student and R.A. @ MIT, USA for technical discussions at various stages of this research.

Author contribution statement

Kazi Tawseef Rahman: Methodology, Investigation, Validation, Data curation, Software, Visualization, Formal analysis, Writing – original draft, Writing – review & editing. **Mustofa Sakif Shahriar:** Investigation, Writing – original draft, Writing – review & editing. **Mashaekh Tausif Ehsan:** Methodology, Validation, Writing – review & editing. **Mohammad Nasim Hasan:** Project administration, Conceptualization, Resources, Supervision, Writing - review & editing.

References:

- [1] R.B. Duffey, Sustainable futures using nuclear energy, *Prog. Nucl. Energy* 47 (2005) 535–543. <https://doi.org/10.1016/j.pnucene.2005.05.054>.

- [2] T. Allen, J. Busby, M. Meyer, D. Petti, Materials challenges for nuclear systems, *Mater. Today* 13 (2010) 14–23. [https://doi.org/10.1016/S1369-7021\(10\)70220-0](https://doi.org/10.1016/S1369-7021(10)70220-0).
- [3] E.J. Pickering, A.W. Carruthers, P.J. Barron, S.C. Middleburgh, D.E.J. Armstrong, A.S. Gandy, High-Entropy Alloys for Advanced Nuclear Applications, *Entropy* 23 (2021) 98. <https://doi.org/10.3390/e23010098>.
- [4] B. Gludovatz, A. Hohenwarter, K.V.S. Thurston, H. Bei, Z. Wu, E.P. George, R.O. Ritchie, Exceptional damage-tolerance of a medium-entropy alloy CrCoNi at cryogenic temperatures, *Nat. Commun.* 7 (2016) 10602. <https://doi.org/10.1038/ncomms10602>.
- [5] Y. Zhang, W.-M. Guo, Z.-B. Jiang, Q.-Q. Zhu, S.-K. Sun, Y. You, K. Plucknett, H.-T. Lin, Dense high-entropy boride ceramics with ultra-high hardness, *Scr. Mater.* 164 (2019) 135–139. <https://doi.org/10.1016/j.scriptamat.2019.01.021>.
- [6] B. Ye, T. Wen, M.C. Nguyen, L. Hao, C.-Z. Wang, Y. Chu, First-principles study, fabrication and characterization of (Zr_{0.25}Nb_{0.25}Ti_{0.25}V_{0.25})C high-entropy ceramics, *Acta Mater.* 170 (2019) 15–23. <https://doi.org/10.1016/j.actamat.2019.03.021>.
- [7] S. Xia, Z. Wang, T. Yang, Y. Zhang, Irradiation Behavior in High Entropy Alloys, *J. Iron Steel Res. Int.* 22 (2015) 879–884. [https://doi.org/10.1016/S1006-706X\(15\)30084-4](https://doi.org/10.1016/S1006-706X(15)30084-4).
- [8] Z. Li, K.G. Pradeep, Y. Deng, D. Raabe, C.C. Tasan, Metastable high-entropy dual-phase alloys overcome the strength–ductility trade-off, *Nature* 534 (2016) 227–230. <https://doi.org/10.1038/nature17981>.
- [9] R.B. Nair, H.S. Arora, S. Mukherjee, S. Singh, H. Singh, H.S. Grewal, Exceptionally high cavitation erosion and corrosion resistance of a high entropy alloy, *Ultrason. Sonochem.* 41 (2018) 252–260. <https://doi.org/10.1016/j.ultsonch.2017.09.044>.
- [10] Q. Xing, A.C. Feltrin, F. Akhtar, Processing, microstructure and high temperature dry sliding wear of a Cr-Fe-Hf-Mn-Ti-Ta-V high-entropy alloy based composite, *Mater. Today Commun.* 28 (2021) 102657. <https://doi.org/10.1016/j.mtcomm.2021.102657>.
- [11] Y. Zhang, G.M. Stocks, K. Jin, C. Lu, H. Bei, B.C. Sales, L. Wang, L.K. Béland, R.E. Stoller, G.D. Samolyuk, M. Caro, A. Caro, W.J. Weber, Influence of chemical disorder on energy dissipation and defect evolution in concentrated solid solution alloys, *Nat. Commun.* 6 (2015) 8736. <https://doi.org/10.1038/ncomms9736>.
- [12] R. Li, L. Guo, Y. Liu, Q. Xu, Q. Peng, Irradiation Resistance of CoCrCuFeNi High Entropy Alloy under Successive Bombardment, *Acta Metall. Sin. Engl. Lett.* 36 (2023) 1482–1492. <https://doi.org/10.1007/s40195-023-01577-w>.
- [13] Y. Li, R. Li, Q. Peng, S. Ogata, Reduction of dislocation, mean free path, and migration barriers using high entropy alloy: insights from the atomistic study of irradiation damage of CoNiCrFeMn, *Nanotechnology* 31 (2020). <https://doi.org/10.1088/1361-6528/ab9cf5>.
- [14] Y. Lin, T. Yang, L. Lang, C. Shan, H. Deng, W. Hu, F. Gao, Enhanced radiation tolerance of the Ni-Co-Cr-Fe high-entropy alloy as revealed from primary damage, *Acta Mater.* 196 (2020) 133–143. <https://doi.org/10.1016/j.actamat.2020.06.027>.
- [15] L. Lang, H. Deng, J. Tao, T. Yang, Y. Lin, W. Hu, Comparison of formation and evolution of radiation-induced defects in pure Ni and Ni–Co–Fe medium-entropy alloy, *Chin. Phys. B* 31 (2022) 126102. <https://doi.org/10.1088/1674-1056/ac891e>.
- [16] H. Yaykaşlı, H. Eskalen, Y. Kavun, M. Göğebakan, A.H. Kaya, Microstructure and Thermal and Radiation Shielding Properties of CoCrFeNiAg High Entropy Alloy, *J. Mater. Eng. Perform.* (2023). <https://doi.org/10.1007/s11665-023-08598-7>.

- [17] R. Zhang, S. Zhao, J. Ding, Y. Chong, T. Jia, C. Ophus, M. Asta, R.O. Ritchie, A.M. Minor, Short-range order and its impact on the CrCoNi medium-entropy alloy, *Nature* 581 (2020) 283–287. <https://doi.org/10.1038/s41586-020-2275-z>.
- [18] L. Zhou, Q. Wang, J. Wang, X. Chen, P. Jiang, H. Zhou, F. Yuan, X. Wu, Z. Cheng, E. Ma, Atomic-scale evidence of chemical short-range order in CrCoNi medium-entropy alloy, *Acta Mater.* 224 (2022) 117490. <https://doi.org/10.1016/j.actamat.2021.117490>.
- [19] Q.-J. Li, H. Sheng, E. Ma, Strengthening in multi-principal element alloys with local-chemical-order roughened dislocation pathways, *Nat. Commun.* 10 (2019) 3563. <https://doi.org/10.1038/s41467-019-11464-7>.
- [20] S.D. Wang, X.J. Liu, Z.F. Lei, D.Y. Lin, F.G. Bian, C.M. Yang, M.Y. Jiao, Q. Du, H. Wang, Y. Wu, S.H. Jiang, Z.P. Lu, Chemical short-range ordering and its strengthening effect in refractory high-entropy alloys, *Phys. Rev. B* 103 (2021) 104107. <https://doi.org/10.1103/PhysRevB.103.104107>.
- [21] J. Ding, Q. Yu, M. Asta, R.O. Ritchie, Tunable stacking fault energies by tailoring local chemical order in CrCoNi medium-entropy alloys, *Proc. Natl. Acad. Sci.* 115 (2018) 8919–8924. <https://doi.org/10.1073/pnas.1808660115>.
- [22] G. Laplanche, S. Berglund, C. Reinhart, A. Kostka, F. Fox, E.P. George, Phase stability and kinetics of σ -phase precipitation in CrMnFeCoNi high-entropy alloys, *Acta Mater.* 161 (2018) 338–351. <https://doi.org/10.1016/j.actamat.2018.09.040>.
- [23] F. He, Z. Wang, Q. Wu, J. Li, J. Wang, C.T. Liu, Phase separation of metastable CoCrFeNi high entropy alloy at intermediate temperatures, *Scr. Mater.* 126 (2017) 15–19. <https://doi.org/10.1016/j.scriptamat.2016.08.008>.
- [24] F.X. Zhang, S. Zhao, K. Jin, H. Xue, G. Velisa, H. Bei, R. Huang, J.Y.P. Ko, D.C. Pagan, J.C. Neumeier, W.J. Weber, Y. Zhang, Local Structure and Short-Range Order in a NiCoCr Solid Solution Alloy, *Phys. Rev. Lett.* 118 (2017) 205501. <https://doi.org/10.1103/PhysRevLett.118.205501>.
- [25] L. Liu, X. Liu, Q. Du, H. Wang, Y. Wu, S. Jiang, Z. Lu, Local chemical ordering and its impact on radiation damage behavior of multi-principal element alloys, *J. Mater. Sci. Technol.* 135 (2023) 13–25. <https://doi.org/10.1016/j.jmst.2022.05.062>.
- [26] Y. Li, J.-P. Du, P. Yu, R. Li, S. Shinzato, Q. Peng, S. Ogata, Chemical ordering effect on the radiation resistance of a CoNiCrFeMn high-entropy alloy, *Comput. Mater. Sci.* 214 (2022) 111764. <https://doi.org/10.1016/j.commatsci.2022.111764>.
- [27] L. Koch, F. Granberg, T. Brink, D. Utt, K. Albe, F. Djurabekova, K. Nordlund, Local segregation versus irradiation effects in high-entropy alloys: Steady-state conditions in a driven system, *J. Appl. Phys.* 122 (2017) 105106. <https://doi.org/10.1063/1.4990950>.
- [28] C. Li, X. Hu, T. Yang, N.K. Kumar, B.D. Wirth, S.J. Zinkle, Neutron irradiation response of a Co-free high entropy alloy, *J. Nucl. Mater.* 527 (2019) 151838. <https://doi.org/10.1016/j.jnucmat.2019.151838>.
- [29] C. Wang, L. Guo, R. Li, Q. Peng, Atomistic Insights into the Irradiation Resistance of Co-Free High Entropy Alloy FeMnNiCr, *Acta Metall. Sin. Engl. Lett.* (2024). <https://doi.org/10.1007/s40195-024-01738-5>.
- [30] Y. Lei, N. Hashimoto, I. Shigehito, Cu-Containing High Entropy Alloys for Nuclear Fusion Application, (2020). <https://doi.org/10.2320/matertrans.MT-M2020049>.
- [31] T. Cicero, M. Jimenez, G. D’Amico, J.A. Pou, G. Dellopoulos, E. Alvaro, S. Cardenas, S. Banetta, B. Bellin, F. Zacchia, B. Calcagno, P. Chappuis, S. Gicquel, R. Mitteau, R.

- Raffray, Progress in the design of Normal Heat Flux First Wall panels for ITER, *Fusion Eng. Des.* 98–99 (2015) 1256–1262. <https://doi.org/10.1016/j.fusengdes.2015.01.023>.
- [32] C. Du, L. Hu, Q. Pan, K. Chen, P. Zhou, G. Wang, Effect of Cu on the strengthening and embrittlement of an FeCoNiCr- x Cu HEA, *Mater. Sci. Eng. A* 832 (2022) 142413. <https://doi.org/10.1016/j.msea.2021.142413>.
- [33] A.P. Thompson, H.M. Aktulga, R. Berger, D.S. Bolintineanu, W.M. Brown, P.S. Crozier, P.J. In 't Veld, A. Kohlmeyer, S.G. Moore, T.D. Nguyen, R. Shan, M.J. Stevens, J. Tranchida, C. Trott, S.J. Plimpton, LAMMPS - a flexible simulation tool for particle-based materials modeling at the atomic, meso, and continuum scales, *Comput. Phys. Commun.* 271 (2022) 108171. <https://doi.org/10.1016/j.cpc.2021.108171>.
- [34] P. Hirel, AtomsK: A tool for manipulating and converting atomic data files, *Comput. Phys. Commun.* 197 (2015) 212–219. <https://doi.org/10.1016/j.cpc.2015.07.012>.
- [35] D.R. Tramontina, O.R. Deluigi, R. Pinzón, J. Rojas-Nunez, F.J. Valencia, R.C. Pasianot, S.E. Baltazar, R.I. Gonzalez, E.M. Bringa, Probing radiation resistance in simulated metallic core–shell nanoparticles, *Comput. Mater. Sci.* 227 (2023) 112304. <https://doi.org/10.1016/j.commatsci.2023.112304>.
- [36] G. Bonny, R.C. Pasianot, N. Castin, L. Malerba, Ternary Fe–Cu–Ni many-body potential to model reactor pressure vessel steels: First validation by simulated thermal annealing, *Philos. Mag.* 89 (2009) 3531–3546. <https://doi.org/10.1080/14786430903299824>.
- [37] J.F. Ziegler, J.P. Biersack, The Stopping and Range of Ions in Matter, in: D.A. Bromley (Ed.), *Treatise Heavy-Ion Sci. Vol. 6 Astrophys. Chem. Condens. Matter*, Springer US, Boston, MA, 1985: pp. 93–129. https://doi.org/10.1007/978-1-4615-8103-1_3.
- [38] J.M. Cowley, An Approximate Theory of Order in Alloys, *Phys. Rev.* 77 (1950) 669–675. <https://doi.org/10.1103/PhysRev.77.669>.
- [39] K. Sheriff, Y. Cao, R. Freitas, Chemical-motif characterization of short-range order with E(3)-equivariant graph neural networks, *Npj Comput. Mater.* 10 (2024) 215. <https://doi.org/10.1038/s41524-024-01393-5>.
- [40] S. Chen, Z.H. Aitken, S. Pattamatta, Z. Wu, Z.G. Yu, D.J. Srolovitz, P.K. Liaw, Y.-W. Zhang, Simultaneously enhancing the ultimate strength and ductility of high-entropy alloys via short-range ordering, *Nat. Commun.* 12 (2021) 4953. <https://doi.org/10.1038/s41467-021-25264-5>.
- [41] E10 Committee, Practice for Neutron Radiation Damage Simulation by Charged-Particle Irradiation, (n.d.). <https://doi.org/10.1520/E0521-96>.
- [42] S. Nosé, A molecular dynamics method for simulations in the canonical ensemble, *Mol. Phys.* 52 (1984) 255–268. <https://doi.org/10.1080/00268978400101201>.
- [43] W.G. Hoover, Canonical dynamics: Equilibrium phase-space distributions, *Phys. Rev. A* 31 (1985) 1695–1697. <https://doi.org/10.1103/PhysRevA.31.1695>.
- [44] J.F. Ziegler, M.D. Ziegler, J.P. Biersack, SRIM - The stopping and range of ions in matter (2010), *Nucl. Instrum. Methods Phys. Res. B* 268 (2010) 1818–1823. <https://doi.org/10.1016/j.nimb.2010.02.091>.
- [45] K. Vörtler, N. Juslin, G. Bonny, L. Malerba, K. Nordlund, The effect of prolonged irradiation on defect production and ordering in Fe–Cr and Fe–Ni alloys, *J. Phys. Condens. Matter* 23 (2011) 355007. <https://doi.org/10.1088/0953-8984/23/35/355007>.
- [46] A. Stukowski, Visualization and analysis of atomistic simulation data with OVITO—the Open Visualization Tool, *Model. Simul. Mater. Sci. Eng.* 18 (2009) 015012. <https://doi.org/10.1088/0965-0393/18/1/015012>.

- [47] B. Widom, Some Topics in the Theory of Fluids, *J. Chem. Phys.* 39 (1963) 2808–2812. <https://doi.org/10.1063/1.1734110>.
- [48] K. Ferasat, Y.N. Osetsky, A.V. Barashev, Y. Zhang, Z. Yao, L.K. Béland, Accelerated kinetic Monte Carlo: A case study; vacancy and dumbbell interstitial diffusion traps in concentrated solid solution alloys, *J. Chem. Phys.* 153 (2020) 074109. <https://doi.org/10.1063/5.0015039>.
- [49] S. Zhao, G.M. Stocks, Y. Zhang, Defect energetics of concentrated solid-solution alloys from ab initio calculations: Ni_{0.5}Co_{0.5}, Ni_{0.5}Fe_{0.5}, Ni_{0.8}Fe_{0.2} and Ni_{0.8}Cr_{0.2}, *Phys. Chem. Chem. Phys.* 18 (2016) 24043–24056. <https://doi.org/10.1039/C6CP05161H>.
- [50] G. Henkelman, B.P. Uberuaga, H. Jónsson, A climbing image nudged elastic band method for finding saddle points and minimum energy paths, *J. Chem. Phys.* 113 (2000) 9901–9904. <https://doi.org/10.1063/1.1329672>.
- [51] J.D. Tucker, T.R. Allen, D. Morgan, Ab initio defect properties for modeling radiation-induced segregation in Fe-Ni-Cr alloys, in: *Proc Int Symp Env. Degradat Mater Nucl Power Syst 13th Whistler BC Can Apr 19*, Citeseer, 2007: pp. 1004–14. <https://citeseerx.ist.psu.edu/document?repid=rep1&type=pdf&doi=2efbb9cacef9fb89ddd1937854dcdafabf6cb1c2> (accessed September 27, 2024).
- [52] O.R. Deluigi, R.C. Pasianot, F.J. Valencia, A. Caro, D. Farkas, E.M. Bringa, Simulations of primary damage in a High Entropy Alloy: Probing enhanced radiation resistance, *Acta Mater.* 213 (2021) 116951. <https://doi.org/10.1016/j.actamat.2021.116951>.
- [53] H. Arkoub, M. Jin, Impact of chemical short-range order on radiation damage in Fe-Ni-Cr alloys, *Scr. Mater.* 229 (2023) 115373. <https://doi.org/10.1016/j.scriptamat.2023.115373>.
- [54] M.W. Ullah, Y. Zhang, N. Sellami, A. Debelle, H. Bei, W.J. Weber, Evolution of irradiation-induced strain in an equiatomic NiFe alloy, *Scr. Mater.* 140 (2017) 35–39. <https://doi.org/10.1016/j.scriptamat.2017.06.042>.
- [55] M. Jin, P. Cao, M.P. Short, Thermodynamic mixing energy and heterogeneous diffusion uncover the mechanisms of radiation damage reduction in single-phase Ni-Fe alloys, *Acta Mater.* 147 (2018) 16–23. <https://doi.org/10.1016/j.actamat.2017.12.064>.
- [56] H. Ullmaier, ed., *Atomic Defects in Metals*, Springer-Verlag, Berlin/Heidelberg, 1991. <https://doi.org/10.1007/b37800>.
- [57] P. Cao, How Does Short-Range Order Impact Defect Kinetics in Irradiated Multiprincipal Element Alloys?, *Acc. Mater. Res.* 2 (2021) 71–74. <https://doi.org/10.1021/accountsmr.0c00102>.
- [58] D. Gaertner, J. Kottke, G. Wilde, S.V. Divinski, Y. Chumlyakov, Tracer diffusion in single crystalline CoCrFeNi and CoCrFeMnNi high entropy alloys, *J. Mater. Res.* 33 (2018) 3184–3191. <https://doi.org/10.1557/jmr.2018.162>.
- [59] J. Ma, S.-H. Wei, Origin of Novel Diffusions of Cu and Ag in Semiconductors: The Case of CdTe, *Phys. Rev. Lett.* 110 (2013) 235901. <https://doi.org/10.1103/PhysRevLett.110.235901>.
- [60] E. Levo, F. Granberg, C. Fridlund, K. Nordlund, F. Djurabekova, Radiation damage buildup and dislocation evolution in Ni and equiatomic multicomponent Ni-based alloys, *J. Nucl. Mater.* 490 (2017) 323–332. <https://doi.org/10.1016/j.jnucmat.2017.04.023>.
- [61] S. Taller, G. VanCoevering, B.D. Wirth, G.S. Was, Predicting structural material degradation in advanced nuclear reactors with ion irradiation, *Sci. Rep.* 11 (2021) 2949. <https://doi.org/10.1038/s41598-021-82512-w>.

- [62] T.M. Smith, M.S. Hooshmand, B.D. Esser, F. Otto, D.W. McComb, E.P. George, M. Ghazisaeidi, M.J. Mills, Atomic-scale characterization and modeling of 60° dislocations in a high-entropy alloy, *Acta Mater.* 110 (2016) 352–363. <https://doi.org/10.1016/j.actamat.2016.03.045>.
- [63] W.-R. Jian, Z. Xie, S. Xu, Y. Su, X. Yao, I.J. Beyerlein, Effects of lattice distortion and chemical short-range order on the mechanisms of deformation in medium entropy alloy CoCrNi, *Acta Mater.* 199 (2020) 352–369. <https://doi.org/10.1016/j.actamat.2020.08.044>.
- [64] E.M. Schulson, The ordering and disordering of solid solutions under irradiation, *J. Nucl. Mater.* 83 (1979) 239–264. [https://doi.org/10.1016/0022-3115\(79\)90610-X](https://doi.org/10.1016/0022-3115(79)90610-X).
- [65] B. Gómez-Ferrer, I. García-Cortés, J.F. Marco, D. Jiménez-Rey, R. Vila, Decoupling of defect and short-range order contributions to resistivity recovery measurements in binary alloys, *Phys. Rev. B* 90 (2014) 220102. <https://doi.org/10.1103/PhysRevB.90.220102>.

List of Tables

Table 1 Recombination rates of Ni, RSS and LCO structures

Table 1. Recombination rates of Ni, RSS and LCO structures

	N_{peak}	N_{end}	% Recombination
Ni	154	16	89.61
RSS	368	13	96.47
LCO	287	14	95.12

List of Figure Captions

- Fig. 1** (a) Transient potential energy of FeNiCu system. (b) Warren-Cowley parameters calculated for the first nearest neighbor shell of the RSS and LCO configurations FeNiCu alloy. (c) Representative configuration of pure Ni, RSS, and LCO systems.
- Fig. 2** (a) Transient variation of number of Frenkel Pairs (N_{FP}), during the first cascade. (b) Variation of N_{FP} versus number of cascades (N_C) with the shaded bands indicating standard deviations.
- Fig. 3** (a-c) Vacancy formation energy (E_f^v) of Fe, Ni, and Cu respectively in RSS. (d-f) E_f^v of Fe, Ni, and Cu respectively in LCO. (g) Vacancy migration energies (E_m^v) in RSS. (h) E_m^v in LCO.
- Fig. 4** (a) Interstitial dumbbell [100] formation energies (E_f^i) and (b) average interstitial dumbbell migration energies (E_m^i) of X-Cu-Y, X-Fe-Y and X-Ni-Y migrations (where X, Y = Cu/Fe/Ni) in RSS and LCO indicated as Cu, Fe, and Ni respectively. The total average migration energy is also shown for comparison. Constant energies for pure Ni are shown as dotted lines in both plots.
- Fig. 5** Size evolution of point defect clusters as a function of N_C in Ni, RSS, and LCO configurations (N_{int} : number of interstitials in interstitial clusters, N_{vac} : number of vacancies in vacancy clusters). (a–d) For interstitial clusters while (e–h) for vacancy clusters. The numbers in brackets in each figure represent the cluster size range.
- Fig. 6** Size evolution of the largest clusters as a function of N_C in the RSS and LCO configurations. (a) Interstitial clusters and (b) vacancy clusters.
- Fig. 7** Snapshots of spatial distribution of point defects and dislocations in (a) RSS after 100, 300, and 500 cumulative cascades (b) LCO after 100, 300, and 500 cumulative cascades (c) Ni after 100, 300, and 500 cumulative cascades.
- Fig. 8** The dislocation densities of total length of dislocation lines with the number of cumulative cascades in RSS and LCO. (a) All dislocation lines and (b) stair-rod dislocation.
- Fig. 9** Snapshots of the system showing dislocation distribution with enlarged view of the circled regions in (a) RSS and (b) LCO systems.
- Fig. 10** (a) MSD as a function of number of cascades (N_C) in Ni, RSS and LCO. (b) Warren Cowley parameter of Cu-Cu pair (α_{Cu-Cu}) as a function of N_C in both RSS and LCO. Percent constituents in interstitial clusters (size > 1) as a function of N_C in (c) RSS and (d) LCO.
-

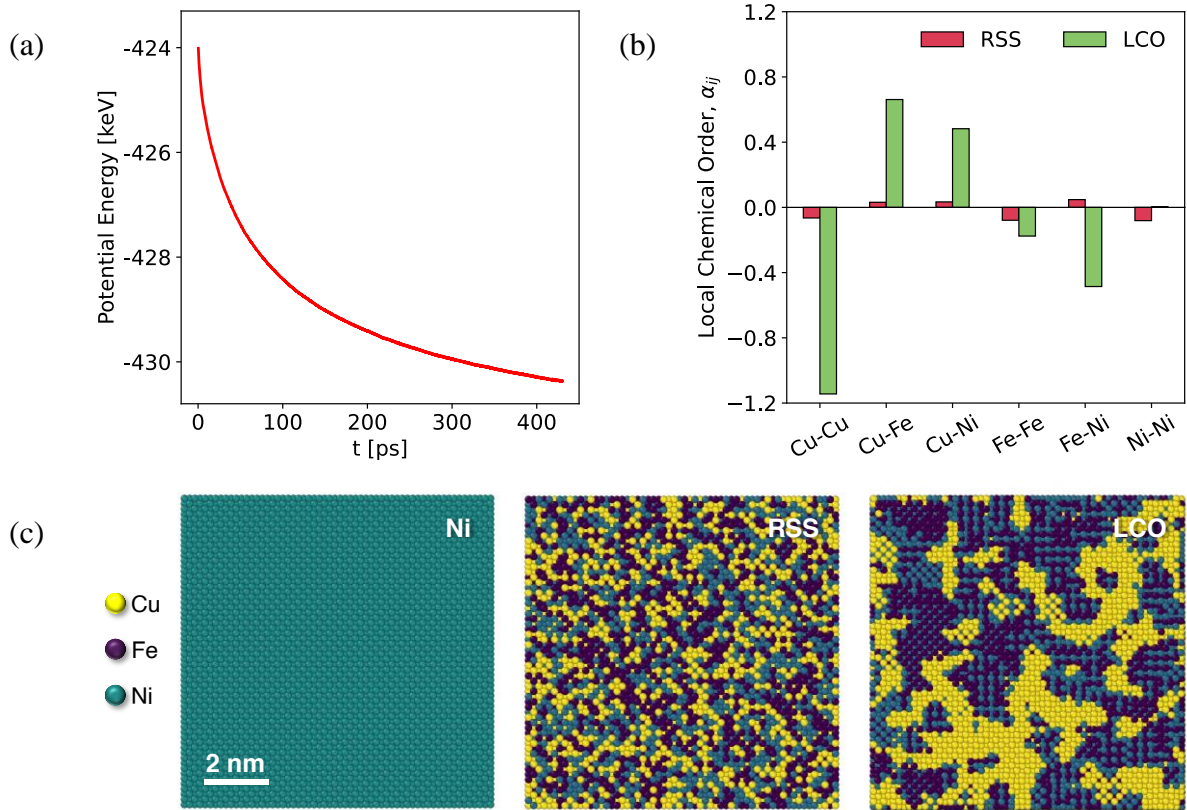


Fig. 1. (a) Transient potential energy of FeNiCu system. (b) Warren-Cowley parameters calculated for the first nearest neighbor shell of the RSS and LCO configurations FeNiCu alloy. (c) Representative configuration of pure Ni, RSS, and LCO systems.

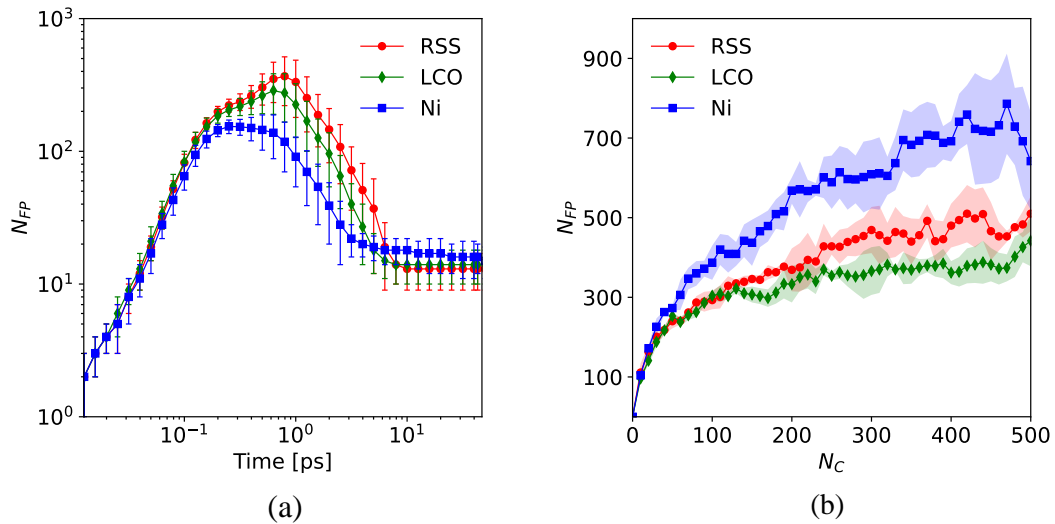


Fig. 2. (a) Transient variation of number of Frenkel Pairs (N_{FP}), during the first cascade. (b) Variation of N_{FP} versus number of cascades (N_C) with the shaded bands indicating standard deviations.

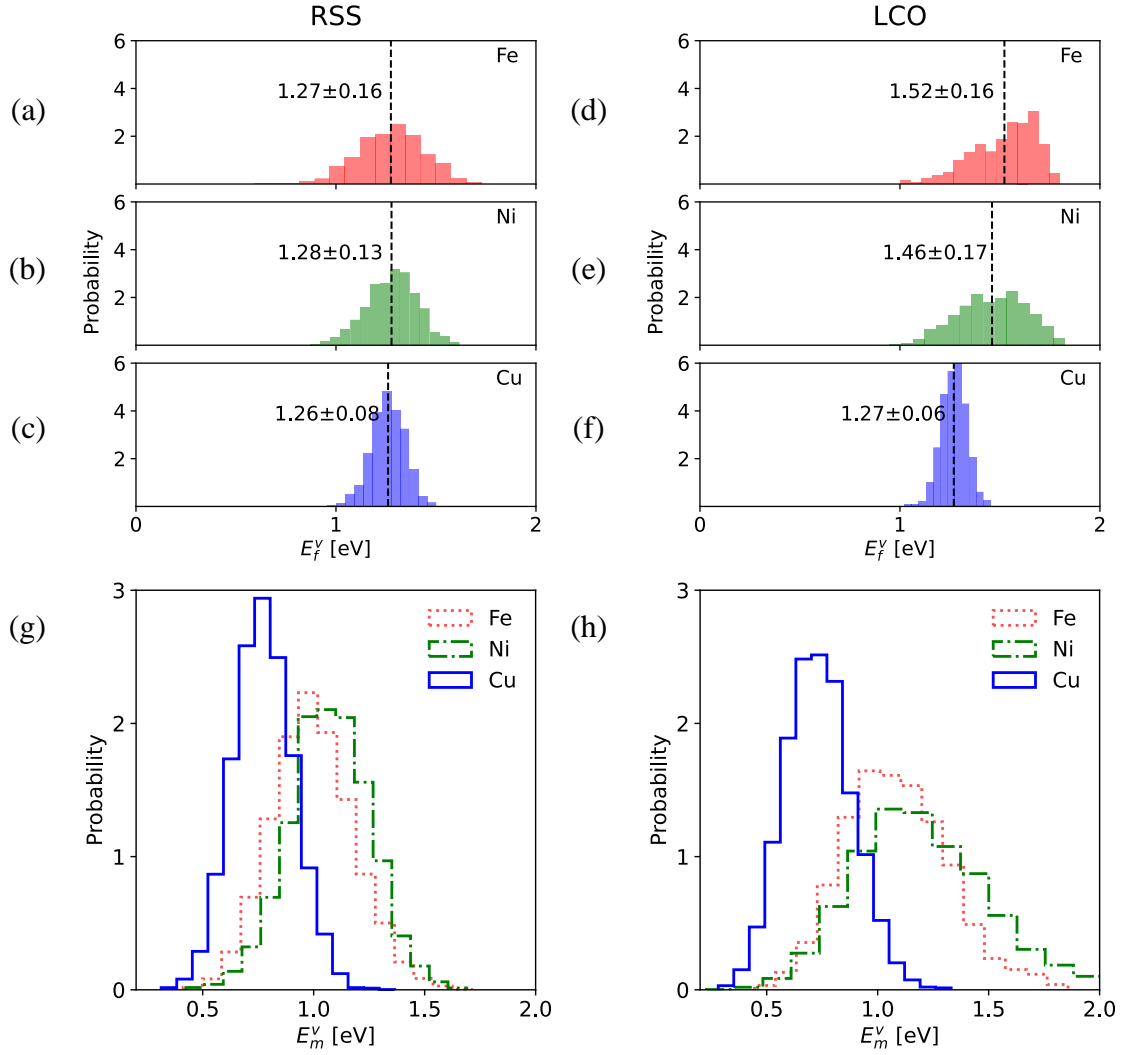


Fig. 3. (a-c) Vacancy formation energy (E_f^v) of Fe, Ni, and Cu respectively in RSS. (d-f) E_f^v of Fe, Ni, and Cu respectively in LCO. (g) Vacancy migration energies (E_m^v) in RSS. (h) E_m^v in LCO.

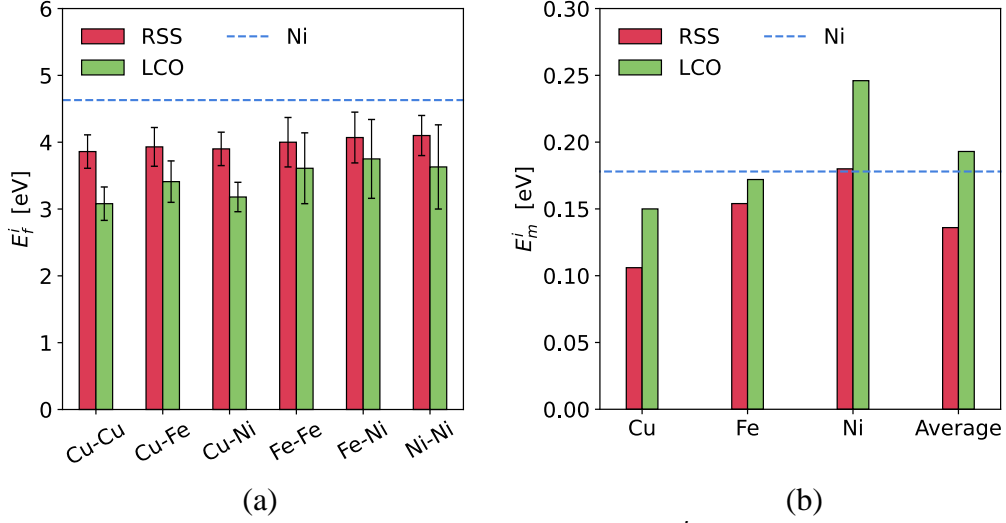


Fig. 4. (a) Interstitial dumbbell [100] formation energies (E_f^i) and (b) average interstitial dumbbell migration energies (E_m^i) of X-Cu-Y, X-Fe-Y and X-Ni-Y migrations (where X, Y = Cu/Fe/Ni) in RSS and LCO indicated as Cu, Fe, and Ni respectively. The total average migration energy is also shown for comparison. Constant energies for pure Ni are shown as dotted lines in both plots.

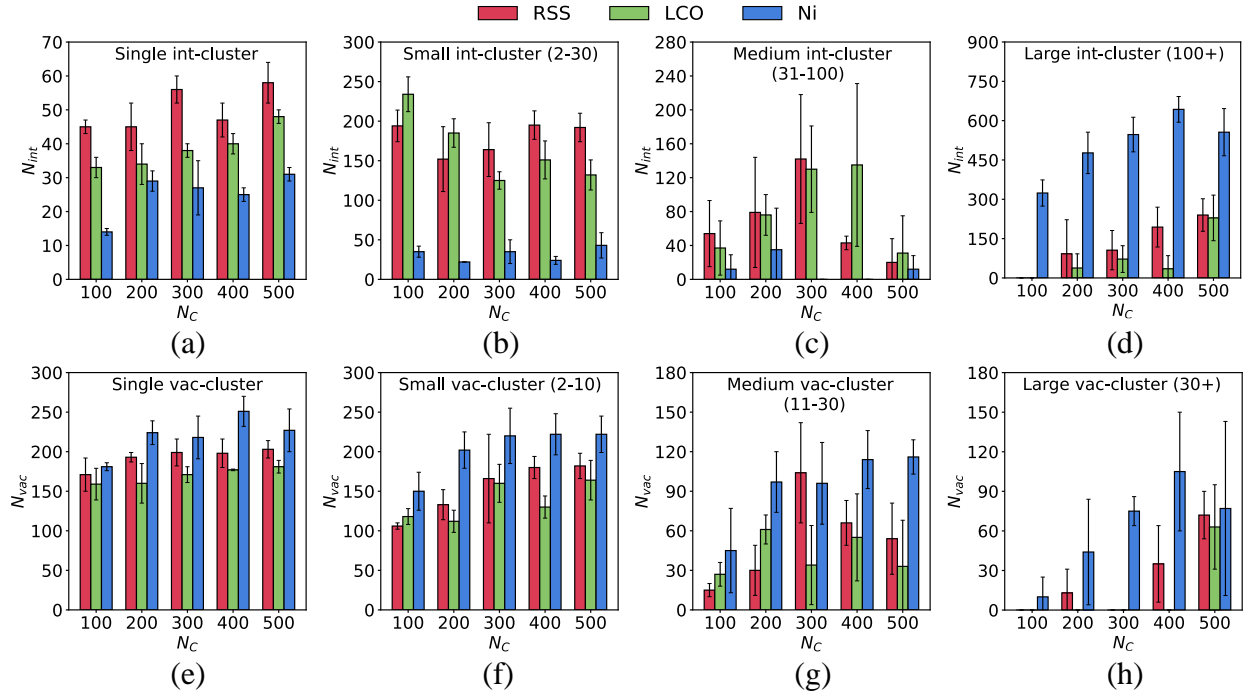


Fig. 5. Size evolution of point defect clusters as a function of N_C in Ni, RSS, and LCO configurations (N_{int} : number of interstitials in interstitial clusters, N_{vac} : number of vacancies in vacancy clusters). (a–d) For interstitial clusters while (e–h) for vacancy clusters. The numbers in brackets in each figure represent the cluster size range.

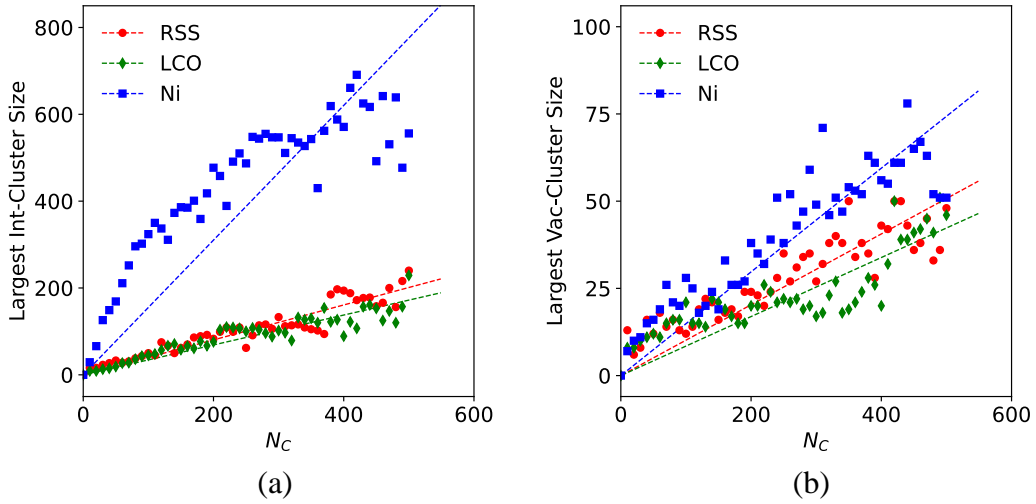


Fig. 6. Size evolution of the largest clusters as a function of N_C in the RSS and LCO configurations. (a) Interstitial clusters and (b) vacancy clusters.

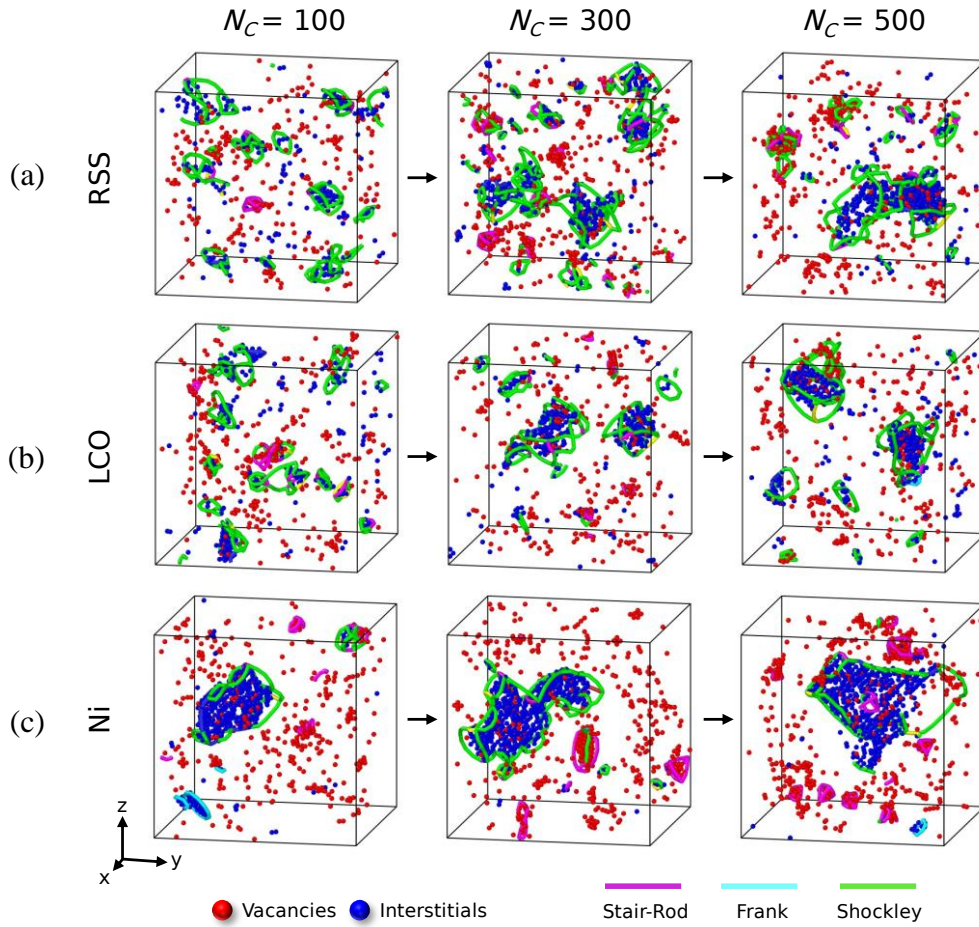


Fig. 7. Snapshots of spatial distribution of point defects and dislocations in (a) RSS after 100, 300, and 500 cumulative cascades (b) LCO after 100, 300, and 500 cumulative cascades (c) Ni after 100, 300, and 500 cumulative cascades.

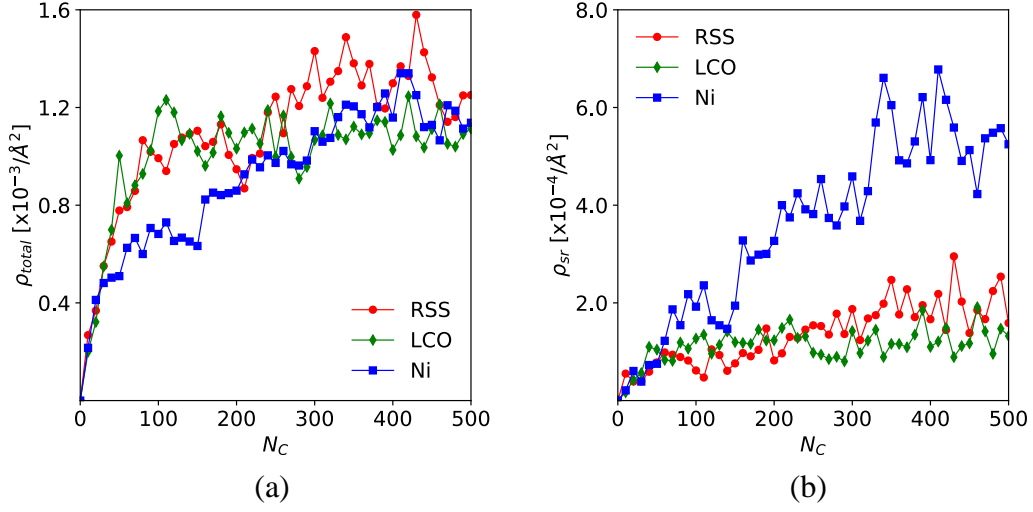


Fig. 8. The dislocation densities of total length of dislocation lines with the number of cumulative cascades in RSS and LCO. (a) All dislocation lines and (b) stair-rod dislocation.

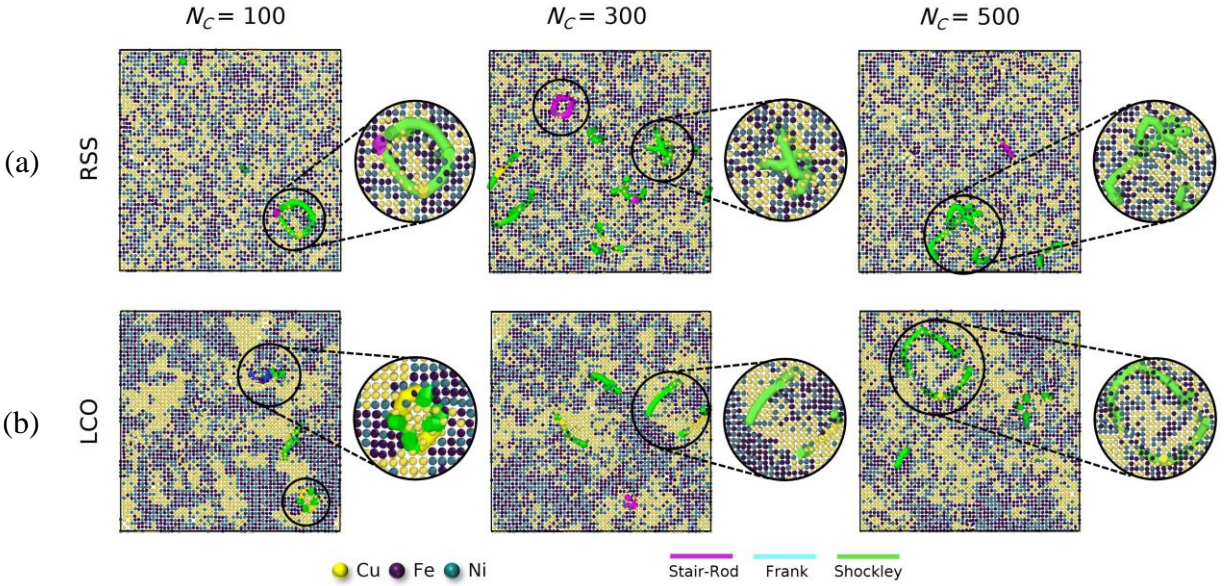


Fig. 9. Snapshots of the system showing dislocation distribution with enlarged view of the circled regions in (a) RSS and (b) LCO systems.

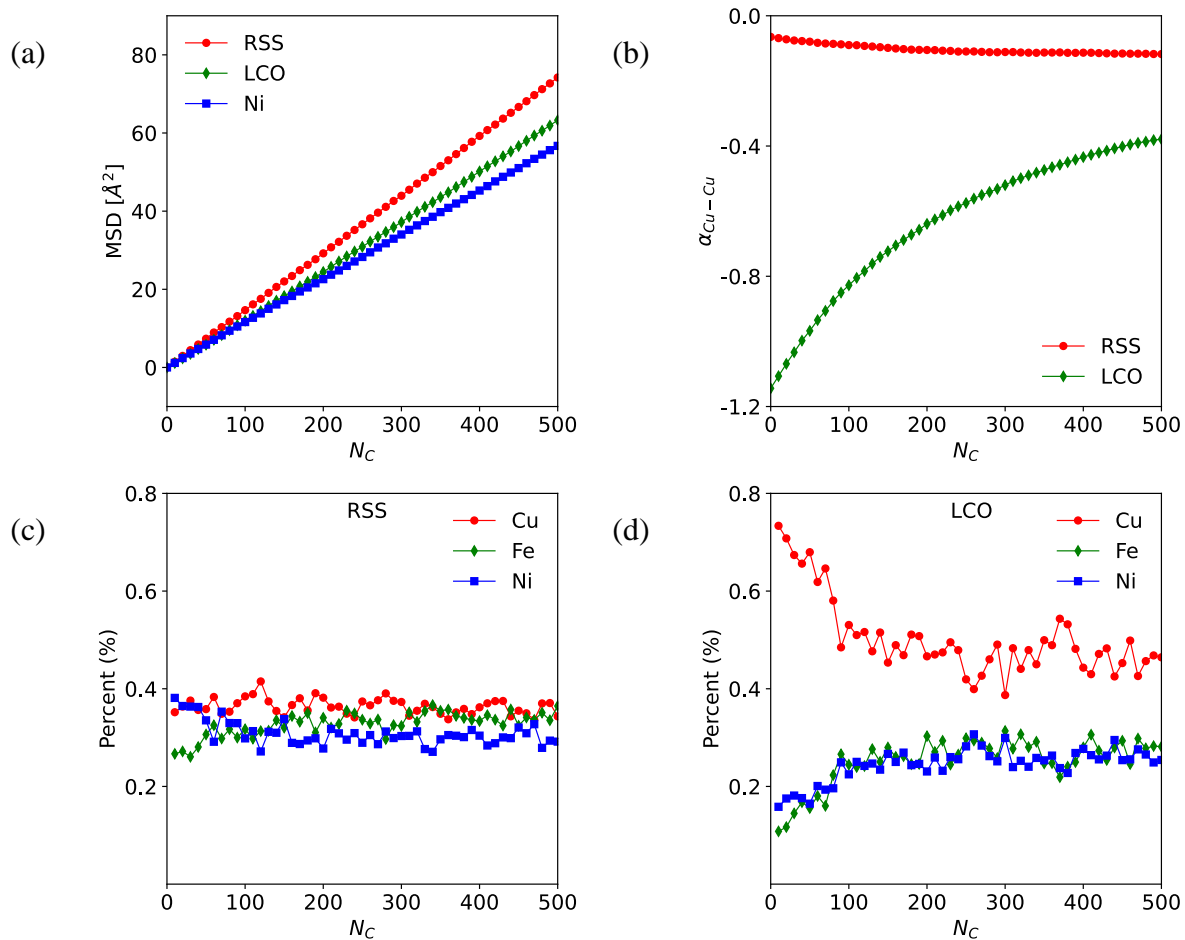


Fig. 10. (a) MSD as a function of number of cascades (N_C) in Ni, RSS and LCO. (b) Warren Cowley parameter of Cu-Cu pair (α_{Cu-Cu}) as a function of N_C in both RSS and LCO. Percent constituents in interstitial clusters (size > 1) as a function of N_C in (c) RSS and (d) LCO.